The Voltage–gated Proton Channel, Hv1, Enhances Brain Damage from Ischemic Stroke

Published as: *Nat Neurosci*. ; 15(4): 565–573.

The Voltage–gated Proton Channel, Hv1, Enhances Brain Damage from Ischemic Stroke

Long–Jun Wu[1,+], **Gongxiong Wu**[2,+], **M. Reza Akhavan Sharif**[3], **Amanda Baker**[4], **Yonghui Jia**[5], **Frederic H. Fahey**[4], **Hongbo R. Luo**[5], **Edward P. Feener**[2], and **David E. Clapham**[1,*]

[1]Howard Hughes Medical Institute, Children's Hospital Boston and Department of Neurobiology, Harvard Medical School, Boston, MA 02115, USA

[2]Research Division, Joslin Diabetes Center, Harvard Medical School, Boston, MA 02215, USA

[3]Department of Radiology, Beth Israel Deaconess Medical Center, Boston, MA, 02115, USA

[4]Department of Radiology, Children's Hospital Boston, Boston, MA, 02115, USA

[5]Department of Lab Medicine, Children's Hospital Boston, and Department of Pathology, Harvard Medical School, Boston, MA, 02115, USA

SUMMARY

Phagocytic cell NADPH oxidase (NOX) generates reactive oxygen species (ROS) as part of innate immunity. Unfortunately, ischemia can also induce this pathway and inflict damage on native cells. Here we show that NOX–mediated damage can be inhibited by suppression of the voltage-gated proton channel, Hv1. Hv1 is required for full NOX activity since it compensates for loss of NOX–exported charge. We show that Hv1 is required for NOX–dependent ROS generation in brain microglia *in situ* and *in vivo*. Mouse and human brain microglia, but not neurons or astrocytes, express large Hv1-mediated currents. Mice lacking Hv1 were protected from NOX–mediated neuronal death and brain damage 24 hours after stroke. These results demonstrate that Hv1–dependent ROS production is responsible for a significant fraction of brain damage at early time points after ischemic stroke and provide a rationale for Hv1 as a therapeutic target for the treatment of ischemic stroke.

INTRODUCTION

During ischemia, reactive molecules containing oxygen (reactive oxygen species, ROS) are produced that rapidly react with lipids, proteins, cofactors and DNA, in turn activating apoptotic pathways[1]. Recent clinical trials with antioxidants, however, are disappointing[2]. Among several sources of oxidative stress in the brain, NADPH oxidase (NOX) is a membrane–bound enzyme that is abundantly expressed in phagocytic cells, including microglia[3]. NOX-mediated ROS production may have evolved as a defense against invading bacteria, but it nonselectively damages cells such as neurons and glia[4]. NOX and ROS are

[*]**Correspondence:** David E. Clapham MD, PhD., Howard Hughes Medical Institute, Children's Hospital Boston, 1309 Enders Research Building, 320 Longwood Avenue, Boston, MA 02115, Phone: 617-919-2680, Fax: 617-731-0787, dclapham@enders.tch.harvard.edu.
[+]Equal Contribution

AUTHOR CONTRIBUTIONS

L.J.W. conducted experiments including electrophysiology, imaging, immunostaining, cell culture, qRT-PCR, Western blot, and MCAO model; G.W. conducted MCAO model, Western blot, immunostaining, qRT-PCR, and cell culture experiments; R.A.S. conducted MRI experiments, A.B. conducted PET/CT experiments. Y.J conducted bone marrow transplantation experiments. L.J.W., G.W., Y.J., F.H.F., and D.E.C. conducted the data analyses; L.J.W. and D.E.C. wrote the manuscript; L.J.W., H.R.L., E.P.F. and D.E.C supervised the project.

consistently reported to participate in the pathogenesis of cerebral ischemia injury; NOX2 or 4 knockout mice exhibit less brain injury after stroke[5, 6]. Thus, reducing NOX–related oxidative stress could ameliorate neuronal damage in ischemic stroke.

NOX transfers electrons across the plasma membrane, rapidly depolarizing and acidifying these cells. As excessive depolarization and intracellular acidification inhibits further expulsion of electrons, a charge–compensating mechanism is needed to maintain NOX activity[7, 8]. By sensing both voltage and pH gradients, Hv1 is ideally suited to the task of charge compensation for NOX activation[9, 10]. Genetic deletion or inhibition of Hv1 greatly reduced NOX–dependent ROS production in leukocytes and bone marrow cells[11, 12]. Therefore, Hv1 is a unique target for controlling multiple NOX activities and ROS production.

Hv1 modulates B–cell activation[13], basophil histamine release[14], and acid secretion from airway epithelium[15] and human spermatozoa[16]. Whether Hv1 is functionally expressed in mammalian brain neurons and glia is unknown, but the early discovery of proton currents in snail neurons has fostered this perception[17]. The presence of voltage–gated proton current *in situ* (*i.e.* within the brain) is debated[18, 19]. Thus, it has not been established whether Hv1 functions *in vivo* in resident brain cells, and if so, whether Hv1 exerts its function through a common NOX mechanism, or whether Hv1 is crucial in oxidative stress–related brain disorders. In this study, we set out to characterize Hv1 in native brain cells and investigate its potential role in neuronal damage in ischemic brain injury.

RESULTS

Hv1 mediates the voltage–gated proton currents in brain microglia

We did not detect Hv1 protein in whole brain lysates when compared to an Hv1–rich tissue such as spleen (Fig. 1a). This raised the question of whether Hv1 is restricted to a particular cell type within brain. Indeed, we found high levels of Hv1 protein in microglia, the principal resident immune response cells in the brain, but not in neurons (Fig. 1b). Quantitative RT–PCR detects Hv1 mRNA in brain and isolated cultured neurons (Suppl. Fig.1). We then examined functional expression of Hv1 in native cells of the brain. Visual identification of microglia was enabled using transgenic mice ($CX3CR1^{GFP/+}$) in which microglia are selectively labeled with GFP (Fig. 1c). A surprisingly large voltage–gated, slowly–activating outward current was recorded in whole–cell patch clamp recordings from microglia in mouse cortical or hippocampal brain slices (Fig. 1d). As is characteristic of Hv1, increasing pH_i decreased outward current and increased the threshold for current activation (Fig. 1d,e). Tail currents were elicited with different pH gradients to estimate the reversal potential (Fig. 1f), differing only marginally from values calculated by the Nernst equation (Fig. 1g) due to proton depletion[7]. Similar proton currents were observed in cortical microglia. Zn^{2+}, the well–established antagonist to Hv1[9, 20], inhibited the proton current in a concentration–dependent manner by shifting V_{thr} to depolarized potentials (Fig. 2a,b). Finally, the voltage–gated proton current was not detected in microglia from Hv1 global knockout ($Hv1^{-/-}$) mice (Fig. 2a,c). These data directly demonstrate that Hv1 is functionally expressed in mouse brain microglia *in situ*.

Previous work reported that proton currents were absent in rat hippocampal microglia[18]. We performed whole–cell recording in hippocampal microglia from rats and mice and found that voltage–gated proton currents are much larger in mice; rat proton current is only 8% of that in mice under our conditions (Suppl. Fig.2; glutamate receptor antagonists were not used during preparation of brain slices). A previous report found that Hv1 was not expressed in mature, but not neonatal mouse brain[11]. However, we found that proton currents are consistently present after birth, exhibiting similar current amplitudes in hippocampal

microglia from P0–2, P7–9 and P21–23 mice (Suppl. Fig.3). Appreciable Hv1 protein and proton–selective currents inhibited by Zn^{2+} were also recorded from cultured human microglia (Fig. 2d–g, Suppl. Fig. 4), and mRNA is detected in microarrays of human brain (http://www.alleninstitute.org). However, it is important to point out the dramatic differences in amplitude between proton current expressed *in situ* (rat microglia in brain slices) and cultured rat microglia[18, 21]. Thus it is not known whether human microglia *in situ* have large Hv1 currents.

Next, we determined whether Hv1 current was present in hippocampal neurons. No measureable voltage–gated proton current was detected, although, we recorded a current that may have been previously misidentified as a proton current[22]. This nonselective ($E_{rev=}0$) outward current was present in $Hv1^{-/-}$ mice (Fig. 2h), was not inhibited by Zn^{2+}, and persisted after increasing intracellular pH from pH_i 5.5 to pH_i 7.2 (Fig. 2h,i). Similarly, we did not observe Hv1 current in cortical neurons from *wt* mice. In addition, no proton currents were detected in astrocytes from young (Fig. 2j) or adult mice (Suppl. Fig. 5). Field recordings performed in the CA1 region of *wt* and $Hv1^{-/-}$ hippocampal slices revealed no difference in the input–output relation of field–stimulated excitatory postsynaptic potentials (fEPSP), paired–pulse facilitation, or high frequency stimulation–induced long–term potentiation (LTP) between *wt* and $Hv1^{-/-}$ mice (Suppl. Fig. 6). Finally, in two learning and memory assays (Y–maze spontaneous alternation and visual discrimination tests), no difference was found between *wt* and $Hv1^{-/-}$ mice (Suppl. Fig. 7). Therefore, we conclude that Hv1 is not present or functionally significant in the neurons or astrocytes we tested, under normal conditions.

Hv1 in acid extrusion and NOX–dependent ROS production in microglia

Hv1 mediates outward proton current that scales with depolarization and the pH gradient. Thus, the Hv1 current is largest when cells are acidified and depolarized. But, does Hv1 regulate H^+ homeostasis under normal conditions? Cultured microglia were acid loaded by the “rebound acidification” technique[23] by perfusing cells with a 20 mM NH_4Cl pulse. The recovery rate of intracellular pH (pH_i) was then calculated. The resting pH_i of microglia was similar in *wt* (7.10 ± 0.05, n=32) and $Hv1^{-/-}$ microglia (7.19 ± 0.03, n=38). After intracellular acidification by NH_4Cl, pH_i recovery rates were similar in *wt* and $Hv1^{-/-}$ microglia in the presence of high Na^+. In contrast, pH_i recovery was abolished in the absence of Na^+ (NMDG replacement) in both *wt* and $Hv1^{-/-}$ microglia (Fig. 3a, b). These results suggest that a Na–dependent mechanism (such as the Na/H exchanger), but not Hv1, mediates acid extrusion during intracellular acidification as low as pH 6.0. However, pH_i rapidly recovers when cells were depolarized with high K^+ solution. The recovery of pH_i was largely reduced in the presence of Zn^{2+} (100 μM) and completely abolished in $Hv1^{-/-}$ microglia (Fig. 3a, b). Therefore, Hv1 is not critical for H^+ homeostasis under resting conditions, but is engaged in microglial acid extrusion upon depolarization.

A well documented function of Hv1 is the transfer of positive charge out of the cytoplasm in compensation for NOX–mediated electron extrusion[7]. Time–lapse confocal imaging was used to measure ROS generation from microglia in the *stratum radiatum* of the hippocampal CA1 region. Again using $CXCR1^{GFP/+}$ mice, dihydroethidium (DHE) was perfused into hippocampal slices and ROS production measured as the oxidation of DHE to ethidium (Fig. 3c). Phorbol ester (PMA) induced the oxidative burst in *wt* brain slice microglia, measured as a slow increase in ethidium fluorescence (Fig. 3c, Suppl. Movie 1). After 20min PMA exposure, fluorescence increased ~8 fold, significantly above that measured from microglia not exposed to PMA (Fig. 3d,e). The increase was abolished by NOX inhibitors, diphenyleneiodonium (DPI, 30 μM) or apocynin (Apo, 300 μM), and by the Hv1 inhibitor, Zn^{2+} (100 μM). Moreover, no significant increase in ethidium fluorescence was found in $Hv1^{-/-}$ microglia after PMA treatment (Fig. 3c–e). PMA did not markedly lower pH_i in *wt*

microglia, but induced significant intracellular acidification in *Hv1*$^{-/-}$ microglia under Na^+–free conditions (Fig. 3f). The PMA–induced intracellular acidification was dependent on NOX activation, as it was inhibited in the presence of DPI (10 μM) (Fig. 3f). These results demonstrate that Hv1 is required for NOX–dependent ROS production and alleviation of NOX–dependent acidification in brain microglia, as has been shown extensively in phagocytic blood cells[13].

Brain microglia extend processes to damaged cells in response to injury signals, such as ATP[24, 25]. To determine whether removal of Hv1 affected this microglial response, time–lapse confocal imaging was used to monitor ATP–induced microglial terminal chemotaxis in acute brain slices from *wt* and *Hv1*$^{-/-}$ mice. The number and speed of hippocampal microglial terminal extensions towards an ATP–containing pipette were indistinguishable between *wt* and *Hv1*$^{-/-}$ mice (Fig. 3g, Suppl. Movie 2). In addition, no difference was found in microglial migration towards TNFα and MCP–1–containing pipettes in cultured microglia from *wt* and *Hv1*$^{-/-}$ mice (Fig. 3h). We conclude that Hv1 is important for microglial ROS production, but is not required for chemotaxis or migration.

Hv1 is critical for brain damage in an ischemic stroke mouse model

NOX is a common mediator of microglia–mediated neuronal damage in stroke[4, 26]. To test whether indirect inhibition of NOX activity by deletion of Hv1 ameliorates ischemic stroke damage, we employed the mouse middle cerebral artery occlusion (MCAO) model. *Wt* and *Hv1*$^{-/-}$ mice were subjected to right–sided permanent ligature MCAO (pMCAO) for 24h under isoflurane anesthesia. The resulting brain injury was estimated by standard 2,3,5–triphenyltetrazolium chloride (TTC) staining, a colorimetric redox indicator that distinguishes metabolically active from inactive tissue (Fig. 4a). The infarct volume in *Hv1*$^{-/-}$ mice was significantly smaller than that in *wt* mice after pMCAO (Fig. 4b). We also found similar reduction of infarct volume in *Hv1*$^{-/-}$ mice compared with that in *wt* mice in initial experiments using ketamine/xylazine as anesthetics (Fig. 4b). The difference in brain damage was functionally relevant, as *Hv1*$^{-/-}$ mice had significantly better neurological scores than *wt* mice (Fig. 4c).

Additional assays for ischemia–induced brain damage were used to further characterize the effect of Hv1 deficiency on the response to pMCAO under ketamine/xylazine anesthesia. First, T2–weighted magnetic resonance imaging (MRI) was used to examine brain injury 24h after pMCAO in *wt* and *Hv1*$^{-/-}$ mice (Fig. 4d). As for TTC staining studies, we found that injury volume in *Hv1*$^{-/-}$ mice was significantly smaller than that in *wt* mice after pMCAO (Fig. 4e, Suppl. Movie 3). Next, positron emission tomography (PET) imaging of 18F–labeled, 2–fluoro–2–deoxy–D–glucose (^{18}F–FDG) uptake, which reflects brain glucose metabolism[27], was examined in *wt* and *Hv1*$^{-/-}$ mice before and 24h after pMCAO. Although there was no difference in ^{18}F–FDG uptake between *wt* and *Hv1*$^{-/-}$ mice before pMCAO, 1d after pMCAO, right hemispheric “cold spots” were significantly smaller in *Hv1*$^{-/-}$ mice (Suppl. Fig. 8a,b). Blood pressure before, and at various time points after pMCAO, did not differ between *wt* and *Hv1*$^{-/-}$ mice (Suppl. Fig. 8c). Brains of wt and *Hv1*$^{-/-}$ mice compared 72h after pMCAO showed a similar degree of protection (Suppl. Fig. 8d,e). Finally, a transient MCAO (tMCAO) stroke model in which mice were subjected to 2h occlusion followed by 22h reperfusion revealed significantly smaller infarct volumes and improved neurological function after tMCAO in *Hv1*$^{-/-}$ mice when compared to *wt* mice (Suppl. Fig. 9a–c). Taken together, these results show that Hv1 supports NOX activity and NOX–induced brain damage, and suggests that inhibition or block of Hv1 will lessen brain damage after stroke. Since we observed similar phenotypes after using isoflurane or ketamine/xylazine as anesthetics in MCAO surgeries, the primary observed effect of Hv1 on brain injury is likely via NMDA receptor–independent mechanisms.

Significantly larger proton currents and lower activation thresholds were recorded from microglia in the ischemic penumbra 24h after pMCAO (Fig. 4f,g). Neither an increase in outward K^+ currents[28] (eliminated by TMA replacement) nor a change in cell membrane area (measured by membrane capacitance) accounted for the increase in outward current (Fig. 4g). We also observed an increase in Hv1 protein in whole brain lysates after stroke (Fig. 4h). Finally, exogenous ROS (H_2O_2) applied to brain slices while recording via the perforated patch method (to preserve physiological intracellular conditions), rapidly enhanced proton currents that were inhibited by $ZnCl_2$ (Suppl. Fig. 10b,c). TRPM2 channels were present in microglia as revealed by intracellular perfusion of ADP ribose[29], but this current was not measurably activated by H_2O_2 perfusion under our conditions (Suppl. Fig. 10a).

Microglial Hv1 contributes to neuronal cell death after ischemia

To directly test whether brain damage was reduced by suppression of Hv1 function, we immunostained the peri–infarct area in *wt* and *Hv1*$^{-/-}$ mice 24h after pMCAO. Significantly larger increases in caspase–3 and TUNEL positive neurons ($NeuN^+$) were found after stroke in *wt* compared to *Hv1*$^{-/-}$ mice (Fig. 5a,b). Similarly, 30min oxygen glucose deprivation (OGD)[30] induced significantly more neuronal death in *wt* microglia/neuronal co–cultures compared to *Hv1*$^{-/-}$ co–cultures (Fig. 5c–e). Cellular necrosis, as indicated by lactate dehydrogenase (LDH) release, was significantly higher in *wt* than *Hv1*$^{-/-}$ microglia–neuron co–cultures after OGD (Fig. 5e). The microglial Hv1–dependent neuronal death is likely due to the NOX activation, as pretreatment of NOX inhibitors, DPI (10 μM) and apocynin (100 μM), significantly reduced microglia–induced neuronal death (Fig. 5f). However, when DPI and apocynin treatments were used after OGD insult, neuronal protection did not reach significance (DPI, mortality from 38.7 ± 3.7% to 31.6 ± 3.6%; apocynin, from 39.6 ± 4.5% to 35.1 ± 3.4%). In addition, microglial Hv1 knockdown by shRNA reduced microglial–dependent neuronal death (Fig. 5f), suggesting that reduced neuronal death after addition of *Hv1*$^{-/-}$ microglia is not due to compensatory effects. Together, these results show that Hv1 supports NOX activation in producing neuronal death after OGD.

NMDA receptor activation enhances neuronal NOX activation and ischemia–induced neurotoxicity[31]. As expected, the NMDA receptor blocker, MK801 (10 μM), protected neurons in both *wt* and *Hv1*$^{-/-}$ neurons (Fig. 5f). NMDA (10 μM, 12 h) induced a similar degree of NO release and cell death in *wt* and *Hv1*$^{-/-}$ neurons (Fig. 5g). NMDA receptor–mediated excitatory postsynaptic currents were not altered in *Hv1*$^{-/-}$ mice compared to *wt* mice (Suppl. Fig. 11). Therefore, reduction of neuronal death in *Hv1*$^{-/-}$ mice was not due to decreased NMDA receptor–mediated excitotoxicity, or to effectors of the NMDA receptor such as NO release.

Microglia Hv1 mediates ROS production after ischemia

During ischemic stroke, microglia release ROS, cytokines, glutamate, and nitric oxide (NO) that increase cell death[32, 33]. Of TNFα, IL–1β, IL6, IFN–γ, VEGF, glutamate, NO, and ROS, we found that only ROS production was reduced in *Hv1*$^{-/-}$ compared to *wt* cultured microglia after OGD (Fig. 6a). ROS production in microglia was also decreased in brain slices after OGD (Fig. 6b; OGD was effective since fEPSPs were largely inhibited in field recordings of hippocampal neurons). In the tMCAO model, both neurons and microglia ipsilateral to the MCAO region exhibited significant increases in ROS production compared with those in the contralateral hemisphere after i.p. injection of DHE in $CX3CR1^{GFP/+}$ mice (Fig. 6c,d). In the cortex and striatum, microglial ROS production was also much smaller in *Hv1*$^{-/-}$ mice than *wt* mice (Fig. 6c,d). Additionally, ipsilateral microglia were more active in *wt* mice, as assayed by an increase in cell body area, compared to those on the contralateral side (Fig. 6c,e). Finally, phosphorylation of the NF–κB subunit, p65 (P–p65), a critical

proinflammatory transcription factor affected by ROS signaling in stroke[34], increased significantly in *wt* mice but not in $Hv1^{-/-}$ mice (Fig. 6f). Together, these results indicate that Hv1 contributes to microglial activation, ROS production, and NF–κB phosphorylation *in vivo* after stroke.

If Hv1 protects brain tissue by reducing NOX–driven ROS during ischemia, ROS scavengers should reduce its effects. EUK–207, a novel mimetic of superoxide dismutase and catalase, is a powerful scavenger in oxidative stress *in vivo* and is effective in alleviating age–related learning deficits[35]. EUK–207 (20 mg/kg), injected at 2 and 24h after pMCAO under ketamine/xylazine anesthesia, reduced the infarction area measured at 72h in both *wt* and $Hv1^{-/-}$ mice (Fig. 6g). Consistent with expectations, the rescue of brain injury by EUK–207 was significantly larger in *wt* than that in $Hv1^{-/-}$ mice (Fig. 6h). The lesser protective effect of EUK–207 in $Hv1^{-/-}$ mice was not due to smaller initial lesions in these mice, as MK801 (1 mg/kg, injected 3 and 6h after pMCAO) was similarly protective in *wt* and $Hv1^{-/-}$ mice 24h after pMCAO under isoflurane anesthesia (Fig. 6h).

Microglial Hv1 contributes to brain damage after stroke

NOX1–5, DUOX1 and DUOX2 are all members of the NOX family[3]. In cultured microglia, only NOX2 mRNA was present at significant levels (Fig. 7a). Western blotting confirmed the expression of NOX2 protein in microglia and brain and similar levels of NOX2 were observed in *wt* and $Hv1^{-/-}$ microglia (Fig. 7b). Most important, there was a significant increase in NOX2 brain expression after pMCAO, or in microglia after OGD (Fig. 7b). These results suggest that NOX2 is the major NADPH oxidase coupled to Hv1 during ROS production.

After stroke, the brain is invaded by blood–borne leukocytes expressing high levels of NADPH oxidase[36]. To test whether peripheral Hv1 also contributes to ischemic injury, four groups of bone marrow chimeric mice (*wt*>*wt*, *wt*>$Hv1^{-/-}$, $Hv1^{-/-}$>*wt*, $Hv1^{-/-}$>$Hv1^{-/-}$ chimeras) were generated and chimeras were subjected to pMCAO 16 days after bone marrow transplantation. Chimeras were confirmed by analyzing overall leukocyte engraftment and neutrophil replacement in recipient mice (Suppl. Fig. 12). We found that 24h after pMCAO, $Hv1^{-/-}$>*wt* mice exhibited similar infarct volumes to those of *wt*>*wt* mice, while *wt*> $Hv1^{-/-}$ mice showed comparable injury to $Hv1^{-/-}$>$Hv1^{-/-}$ mice (Fig. 7c,d). Moreover, there was significantly more brain damage in $Hv1^{-/-}$>*wt* than that in *wt*> $Hv1^{-/-}$ mice (Fig. 7c,d). These results suggest that Hv1 in resident microglia primarily supports NOX–mediated brain damage during early stages of ischemic stroke.

DISCUSSION

We have shown that Hv1 is expressed and functions as the voltage–gated proton–selective current in mouse and cultured human brain microglia. We found that microglial Hv1 is required for NOX–dependent ROS generation both *in vitro* and *in vivo*. Hv1, by rapidly exporting positive charge (H^+), is required for NOX to effectively transport electrons and thus generate ROS. Experimentally induced ischemia or metabolic challenge elicits ROS production from microglia and other inflammatory cells. ROS are not entirely detrimental, as they are also cerebral vasodilators and mediators of tissue repair and remodeling following ischemic injury[37]. Nevertheless, neuronal lipids, membrane receptors, intracellular kinases and phosphatases, as well as pro–apoptotic transcription factors[1] are all targets of ROS that damage brain function (Suppl. Fig. 13).

Our ROS imaging experiments demonstrate that mouse microglial Hv1 is activated and indeed required for the majority of NOX–dependent ROS production by microglia *in situ*. The Hv1 channel is ideally suited for this function since it is activated only upon

depolarization. The amount of depolarization needed is inversely proportional to the pH gradient. Under most physiologically relevant conditions this means that upon cell acidification, less depolarization from rest is required to allow protons to exit the cell, exactly the conditions under which NADPH oxidase is active. Without Hv1, NOX activation will cause significant depolarization and intracellular acidification that will eventually inhibit NOX activation.

One of the many changes defining microglia activation in response to ischemia is translocation of NOX cytosolic subunits to the plasma membrane where it becomes active[32, 34]. Here, we have shown that microglial Hv1 contributes significantly to NOX ROS production, supporting NOX–mediated neuronal cell death after stroke. First, PMA– or OGD–induced ROS production was significantly reduced in $Hv1^{-/-}$ microglia compared with *wt* microglia. Second, ROS production in brain microglia *in situ* after stroke was reduced in $Hv1^{-/-}$ mice. Third, reduced neuronal death and brain damage was observed in $Hv1^{-/-}$ mice compared to *wt* mice after stroke. Fourth, OGD–induced neuronal death in microglia ($Hv1^{-/-}$)–neuron co–cultures was less than that in *wt* co–cultures. Fifth, rescue by ROS scavengers was less in $Hv1^{-/-}$ compared to wt mice. Finally, chimeric mice with *wt* microglia, but $Hv1^{-/-}$ circulating blood cells ($Hv1^{-/-}$>*wt*), showed significantly more brain damage than mice with $Hv1^{-/-}$ microglia and *wt* blood cells (*wt*> $Hv1^{-/-}$), establishing that 24h after stroke, resident microglia are responsible for most of the ROS–mediated brain damage.

All cell types in the brain contain NADPH oxidases and mice deficient in NOX2 or NOX4 have better stoke outcomes[5, 6]. Astrocytes comprise a significant proportion of cells in the brain and express NOX1, 2 and 3[38], but we did not detect Hv1 currents in mouse astrocytes. We assessed brain tissue damage at 1d after MCAO, but large numbers of circulating blood cells enter the brain at later times after stroke[39, 40]. Therefore, we do not exclude the contribution of Hv1 in late stages of stroke. A caveat to the interpretation of bone marrow chimera experiments is the potential complication of irradiation[41]. Nonetheless, it is unlikely that microglia are the only sources of ROS–mediated brain damage since ROS are released from all metabolically stressed mitochondria. Moreover, microglia may exert important protective effects by producing IL–10 and TGF–β, as well as growth factors in the post–ischemic brain[42]. Therefore, the dual protective/destructive effects of microglia should be considered when targeting microglia for stroke treatment.

We found no voltage–gated proton current in hippocampal or cortical neurons in acute brain slices. Moreover, hippocampal basal synaptic transmission, plasticity or NMDA receptor function did not differ between *wt* and $Hv1^{-/-}$ mice. NMDA induced similar degree of cell death in *wt* and $Hv1^{-/-}$ neurons. Thus, glutamate neurotoxicity is unlikely to underlie Hv1's contribution to brain damage. Finally, since Hv1 function is important in peripheral blood cells[13,14], late effects after stroke requires future study.

Currently, therapies for ischemic stroke are limited[43]. Recent studies using NOX inhibitors show conflicting results, perhaps due to poor NOX selectivity[43]. We suggest that Hv1 channels may be more tractable targets for prevention of brain injury during ischemia. Notably, since Hv1 currents below detection levels in neurons, Hv1 inhibitors should not limit neuronal NOX activity. Our results may also be relevant for other ischemic disorders and ROS–related neurodegeneration.

EXPERIMENTAL PROCEDURES

Animals

Hv1$^{-/-}$ mice were back–crossed into C57BL/6 mice for ≥10 generations[12]. Heterozygous *Cx3cr1*$^{GFP/+}$ mice (microglia selectively labeled with GFP[44]) were obtained from Jackson Laboratories. To *Hv1*$^{-/-}$ mice were bred with *Cx3cr1*$^{GFP/+}$ mice to generate *Cx3cr1*$^{GFP/+}$–*Hv1*$^{+/-}$ mice. Littermate *Cx3cr1*$^{GFP/+}$– *Hv1*$^{-/-}$ and *Cx3cr1*$^{GFP/+}$–*Hv1*$^{+/+}$ were obtained by breeding male and female *Cx3cr1*$^{GFP/+}$– *Hv1*$^{+/-}$ mice. We refer to *Cx3cr1*$^{GFP/+}$–*Hv1*$^{+/+}$ as *wt* mice for simplicity. Transgenic mice overexpressing GFP under the control of the astrocyte–specific glial fibrillary acidic protein (GFAP) promoter were from Jackson Laboratories and Sprague–Dawley rats from Charles River Laboratories. Mouse bone marrow chimeras were created from *wt* donor mice to *wt* (*wt*>*wt*) or *Hv1*$^{-/-}$ recipient mice (*wt*> *Hv1*$^{-/-}$) as well as *Hv1*$^{-/-}$ donor mice to *wt* (*Hv1*$^{-/-}$>*wt*) or *Hv1*$^{-/-}$ recipient mice (*Hv1*$^{-/-}$>*Hv1*$^{-/-}$). Whole bone marrow cells from donor of *wt* (CD45.1) or *Hv1*$^{-/-}$ mice (CD45.2) were prepared by flushing the femur and tibia with PBS containing 2% heat-inactivated fetal bovine serum (FBS) under sterile conditions. Red blood cells were lysed (ACK buffer; Gibco). Bone marrow cells (3×10^6 cells) were injected into the lethally γ–irradiated (2× 5.2 Gy, 3h apart) recipient of *wt* (CD45.1 or CD45.2) or *Hv1*$^{-/-}$ mice (CD45.2) via tail vein injection. At 16d post–transplantation, recipient mice were analyzed for total leukocytes and neutrophil engraftment using CD45.1–PE, CD45.2–APC and Gr–1–FITC antibodies with flow cytometry analysis. Experimental procedures were approved by and performed in accordance with guidelines of the Children's Hospital Boston Institutional Animal Care and Use Committee.

Brain slice recordings

Mice and rats were anesthetized with isoflurane and coronal slices (300 μm) of prefrontal cortex or hippocampus prepared[45]. After 1h recovery, brain slices were perfused with oxygenated ACSF solution at 3–4ml/min. In some experiments, NaCl was replaced by $NaMeSO_3$ to eliminate potential Cl^- currents. NaH_2PO_4 was omitted in the ACSF when $ZnCl_2$ was added. Whole–cell patch–clamp recordings in microglia were made using 5–10MΩ glass pipettes filled with TMA–based intracellular solution including (in mM): 100 TMA–$MeSO_3$, 1 EGTA, 100 MES (pH 5.5), Bis–Tris (pH 6.5), or HEPES (pH 7.5); 290–300mOsm. Perforated whole–cell recordings were made on the soma of GFP–labeled microglia using amphotericin B (0.4 mg/ml; Sigma). In perforated whole–cell recordings the pipette solution contained (in mM): K–gluconate, 120; NaCl, 5; $MgCl_2$ 1; EGTA, 0.5; Mg–ATP, 2; Na_3GTP, 0.1; HEPES, 10; pH 7.2; 290–300 mOsm. For hippocampal CA1 neurons, a Cs^+–based internal solution contained (in mM): Cs–$MeSO_3$, 120; NaCl, 5; $MgCl_2$ 1; EGTA, 0.5; Mg–ATP, 2; Na_3GTP, 0.1; HEPES, 10; pH 7.2; 290–300mOsm. Cell morphology was confirmed by Alexa Fluor 594 (50mM). A bipolar tungsten–stimulating electrode was placed in the *stratum radiatum* of the CA1 region and stimulated (Master–8). Holding potential=−60mV. P/N leak subtraction (n=5) minimized current contamination.

Confocal imaging, time–lapse ROS detection and ATP–induced chemotaxis

Confocal microscope (Fluoview FV 300, Olympus) was used to image GFP–labeled microglia (488nm for GFP excitation; 633nm for DIC imaging). DHE (5μM; Sigma), which binds to DNA of $O_2^{-\bullet}$–producing cells, reported ROS production (no pre–incubation). Ethidium fluorescence was elicited by excitation at 543nm and measured at 560nm; GFP–microglia were excited at 488nm and emission collected at 505–600nm. Images were recorded every 5s for 20min. ATP–induced chemotaxis of microglia processes is described previously[25].

pMCAO and tMCAO stroke models

Middle cerebral artery occlusion (MCAO) was carried out as previously described[46] with minor modifications. The stroke study design followed recent international expert recommendations[47]. Age–matched male mice were picked at random without knowledge of genotype. Anesthesia was via intraperitoneal injection of a mixture of ketamine (100mg/kg) and xylazine (20mg/kg) in initial experiments (45–60 min). As ketamine blocks NMDA receptors, which may contribute to brain damage after ischemic stroke, we repeated experiments using the inhalational anesthesia, isoflurane. The mice were anesthetized with 2% isoflurane in 68% nitrous oxide and 30% oxygen and maintained under 1.5% isoflurane during surgery. Temperature was maintained at 37°C using a rectal temperature–regulated heating pad (Kent Scientific). The bregma was exposed and the skull bone countersunk at two 3×3mm areas over both MCA supply territories for bilateral monitoring of local cortical blood flow (Laser Doppler Flowmetry; LDF). The right external carotid artery was transected and a silicone–coated 4–0 monofilament (final diameter 0.28mm) advanced until its tip occluded the origin of the MCA. For tMCAO, reperfusion was initiated by filament withdrawal after 120min. Successful MCAO was defined as uncomplicated filament introduction leading to a steep, sustained ipsilateral LDF decline. Brain blood flow, blood pressure, brain temperature, blood gases, and plasma glucose were measured before and after MCAO. No difference was found between *wt* and $Hv1^{-/-}$ mice. Data from 144 mice (78 *wt* mice and 66 $Hv1^{-/-}$ mice) are included in the final results. A total of 21 *wt* mice (21.2% mortality) and 11 $Hv1^{-/-}$ mice (14.3% mortality) died before completion of the experiment and were excluded from analysis. A total of 17 mice (10 *wt* mice and 7 $Hv1^{-/-}$ mice) were excluded due to the lack of effective occlusion.

Infarct volume and neurological evaluation

24h or 72h after MCAO, mice were anesthetized, the brain frozen at −20°C, cut into five 1–mm coronal sections, and incubated in 2,3,5–triphenyltetrazolium chloride (TTC, 2%; Sigma) solution for 15–20min at 37°C. The stained slices then were transferred into 10% formaldehyde solution. Images of 5 brain sections were recorded (Matrox Intellicam, v 2.0) and analysis of infarct volume blinded to genotype. Intact volumes of ischemic ipsilateral and normal contralateral brain hemispheres were calculated by multiplying the sum of the areas by the distance between sections. Volumes of the infarct were measured indirectly by subtracting the non–ischemic tissue area in the ipsilateral hemisphere from that of the normal contralateral hemisphere. The observer was blinded to mouse genotype; evaluation followed a modified neurological scoring system[48].

In situ ROS detection

DHE histochemistry was performed in tMCAO mice. $CX3CR1^{GFP/+}$ and $CX3CR1^{GFP/+}$–$Hv1^{-/-}$ mice were used to measure microglial ROS production directly, avoiding reduction of ROS fluorescence during immunostaining. 20h after tMCAO, DHE (20 mg/Kg) was injected i.p. at 1h intervals for 2h; 1h after the last injection the mice were anesthetized and perfused intracardially with PBS, followed by 4% paraformaldehyde. Ethidium, DAPI signals, and the area of the microglial cell body were quantified with ImageJ software by masking non–microglial cells. The oxidation of DHE i*n vivo* can generate multiple fluorescent products with overlapping spectra, which may not be exclusively located in the nucleus[49].

MRI

MRI was performed at 4.7 Tesla (BioSpec 47/40; Bruker Biospin) using a transmit/receive birdcage coil (inner diameter, 22mm). Mice were anesthetized (1–2% isoflurane; Florane, Baxter) via a nose cone, and placed in a prone position with the brain centered with respect

to the center of the coil. Multi–slice coronal and axial T2–weighted images of brain were acquired using a rapid spin echo pulse sequence (RARE) with repetition time (TR)=2000ms, echo time (TE)=75ms, matrix size=144×144, number of phase encoded echoes=12, field of view (FOV)=2.56×2.56cm, number of averages (NEX)=16, and slice thickness=1mm. Estimated infarct volume was calculated as 1mm slice thickness × infarct area.

Tissue culture

Brain microglia were isolated from 1–2d–old mice. The cortex was dissected, minced, and dissociated for 15min using 0.125% trypsin (Invitrogen). The cells were seeded into flasks with MEM containing 10% FBS and 100mM gentamicin. The mixed cultures were allowed to grow for 14d and then placed on a shaker for 4h at 200rpm in a standard tissue culture incubator. The supernatant containing detached microglia was centrifuged, the cell pellet re–suspended for counting, and then plated at 10^5 cells/well in 24–well plates, yielding microglia purity >95% verified by immunostaining with the microglial marker Iba–1. Human microglial cells (Clone Express) were isolated from fetal brain tissue and cultured for 3d at 10^5 cells/well in 6–well plate before recordings.

Neurons from E18 mouse cortex were dissociated and plated in neurobasal medium supplemented with B27, 0.5mM glutamine, and 12.5mM glutamate in 6–well plates at 10^6 cells/well. Neurons were switched to maintenance medium (neurobasal medium+B27, 0.5mM glutamine) until ready for experiments at 14–18d *in vitro* (DIV). Under these conditions, >90% of the cells bore the neuronal marker, NeuN; <5% of the cells expressed the astrocytic marker, GFAP. Neuron–microglia co–cultures: microglia (10^5 cells/well, DIV 14) were added to cultured cortical neurons (10^6 cells/well, DIV 10) in 6–well plates.

Intracellular pH (pH_i) measurements

Cultured microglia grown on coverslips were loaded with 2.5μM BCECF/AM for 15min at room temperature. The coverslips were perfused with HCO_3^-–free HEPES–buffered solution containing (in mM): 140 NaCl, 5 KCl, 1 $MgCl_2$, 2 $CaCl_2$, 20 HEPES; pH 7.3. Cells were alternatively illuminated with 440 and 490nm light (Lambda DG–4; Sutter Instruments) for 20–100ms. Images were acquired via a 535±35–nm emission filter on a CCD camera (Orca–ER; Hamamatsu Photonics), and analyzed with Slidebook (Intelligent Imaging Innovations). After background subtraction, the ratio of the 440– and 490nm light excited images was calculated and converted to intracellular pH using the high K^+/nigericin technique[50]. Cells were acid loaded with 20 mM NH_4^+ -containing solution (5min). For Na^+–free solution, NaCl was replaced with NMDG–Cl. For Na^+–free, high K^+ solution, NaCl was replaced with KCl. For calibration, 10μM nigericin was added to solutions containing (in mM):150 KCl, 1 $MgCl_2$, 0.2 EGTA, and 20 HEPES, pH 7.0–8.0, or 20 MES, pH 6.0–6.5. pH_i recovery rate after NH_4^+ treatment was determined from a linear regression fit at pH 6.5.

Immunofluorescence

Mice were anesthetized by i.p. injection of a mixture of ketamine (100mg/kg) and xylazine (20 mg/kg), perfused, and postfixed. Coronal brain sections of 20μm thickness were serially cut through the brain by cryostat. To identify neuronal apoptosis, brain sections were sequentially incubated with rabbit antibody against caspase-3 (1:100, BD Bioscience) and mouse monoclonal antibody directed against NeuN (1:200, Chemicon), and then Rhodamine-conjugated goat anti-rabbit (1:200, Chemicon) and FITC-conjugated goat anti-mouse antibodies. TUNEL (terminal deoxynucleotidyl transferase-mediated uridine 5'-triphosphate-biotin nick end labeling) staining was employed using an *in situ* apoptosis detection kit according to the manufacturer's instructions (Chemicon).

Quantitative real–time PCR

Total RNA was isolated from the mouse brain, spleen, primary microglia or neuronal cells. Real–time PCR was performed using SYBR Green in an iCycler (Bio–Rad). The following primers were used for detecting Hv1 mRNA levels: *Hvcn1 F1*, TGCAAAGGAGTGCTGCAAACTA, *Hvcn1 R1*, TCGAGTAGACGCTCCGCAAT. Primers of NOX1, NOX2, NOX3, NOX4 and 18s rRNA were obtained from Qiagen as RT^2 qPCR primer assays. 18s rRNA was the internal control RNA, data expressed as Ct (cycle threshold), and raw fold–changes normalized to Hv1 mRNA expression in spleen.

Western blotting

Proteins were isolated from the mouse brain, spleen, primary microglia, and neurons. Proteins were separated electrophoretically on 12% polyacrylamide gels and blotted onto PVDF membranes (nonspecific binding blocked by 1h incubation in PBS containing 0.05% Tween 20, and 5% nonfat milk). Affinity–purified polyclonal rabbit antibodies were raised against the keyhole limpet haemocyanin (KLH)–conjugated Hv1 peptide CSEKEQEIERLNKL[9] (α1–Hv1) or obtained from Yuriy Kirichok[16](α2–Hv1). Blots were probed with anti–Hv1 antibodies or mouse anti–mouse β–actin antibody (Cell Signaling). After washing and incubation with secondary horseradish peroxidase–conjugated antibodies (Abcam), membranes were developed (ECL SuperSignal West Pico kit; Pierce). Antibodies: NF–κB subunit P65 and phosphorylated P65 (at Ser 536) from Cell Signaling; NOX2 from Abcam. Densitometry determined protein content; analysis adjusted for equal loading using β–actin.

OGD in culture or brain slices

For oxygen glucose deprivation, cells were rinsed twice and incubated in glucose-free MEM medium. Cultured cells were then introduced into an anaerobic chamber containing a mixture of 95% N_2 and 5% CO_2 at 37°C for 30min. For brain slice OGD, cells were perfused with glucose-free ACSF bubbled with 95% N_2 and 5% CO_2 for ≥ 30min. Switching to normal culture medium or ACSF terminated OGD.

Other cellular assays

To compare migration of *wt* and $Hv1^{-/-}$ microglia cells, 100ng/ml MCP–1 or TNF–α was used as a chemoattractant and added to the conditioned media. A 12–well cell migration assay was used following the manufacturer's instructions (Millipore). Cell mortality in culture after OGD was assessed with the LIVE/DEAD Viability/Cytotoxicity kit (L–3224; Invitrogen). LDH released into the culture medium was measured with the Cytotox 96 nonradioactive cytotoxicity assay kit (Promega). ELISA kits from R&D Systems were used to measure IL–1β, IL–6, TNF–α, IFN–g, or VEGF levels. Absorbance at 450nm was determined in a microplate reader. Glutamate concentration was determined with the Glutamate Assay Kit colorimetric method (Abcam). Griess reagent (R&D Laboratories) was used for NO release detection.

Learning and memory test

Y-maze spontaneous alternation tests were carried out in a white Plexiglas Y-shaped maze (i.e. 3 equidistant arms). All sessions were videotaped and analyzed with LocoScan Software (Clever Sys). At the beginning of the session, mice were placed into the center of the Y-maze and allowed to explore freely for 6 min. Each subject received a single session. The computer-assisted video-tracking system automatically recorded the distance traveled and sequence of arm entries during testing.

PET and CT imaging

Mice were fasted overnight to minimize muscular uptake of ^{18}F-FDG. Between 4.1 and 10.8 MBq (112–292 μCi) were administered by tail vein injection. The mice were then anesthetized with a 2–4% isoflurane/oxygen mixture just prior to imaging. PET images were acquired for 15 min using a Siemens Focus 120 MicroPET. CT was then performed for anatomical correlation using a Siemens MicroCAT II scanner (80 kV with 500 μA and 0.5 s for each of 361 projections over 360°). Regions of interest (ROIs) were centrally placed in each hemisphere and median and mean pixel values within the ROI reported in units of % of injected dose per gram (%ID/g) by dividing the PET values (in Bq/ml) by the injected dose (in Bq). MCAO was induced on the right side so that the ^{18}F-FDG uptake left/right hemisphere (L/R) ratio enabled each animal to serve as its own control.

Flow cytometry analysis

Orbital blood was collected from recipient mice. Red blood cells were lysed by incubation with ACK buffer (Invitrogen) at room temperature for 5 min. Cells were incubated with CD45.1-PE, CD45.2 and Gr-1-FITC antibodies for 45 min on ice. All data were collected on a BD FACSCanto II flow cytometer, and data analysis performed using FlowJo software.

Statistics

Data are expressed as mean ± standard error of the mean (s.e.m.). Statistical comparisons were performed with the Student's t–test. In all cases, $P < 0.05$ was considered statistically significant. * indicates $P<0.05$; **indicates $P<0.01$.

Supplementary Material

Refer to Web version on PubMed Central for supplementary material.

Acknowledgments

We thank Lev Silberstein, Wei Yang, and Martin Kurtev for technical assistance, and Susan Doctrow (Boston University) for kindly providing us EUK–207, Yuriy Kirichok (University of California, San Francisco) for Hv1 antibody, and Dipayan Chaudhuri for critical reading of the manuscript. This work is supported by the National Institutes of Health National Institute of Mental Health (R01–MH090293–01). L–J.W. is supported by a Lefler postdoctoral fellowship from Harvard Medical School and Scientist Development Grant from American Heart Association (11SDG7340011).

REFERENCES

1. Nathan C, Ding A. SnapShot: Reactive Oxygen Intermediates (ROI). Cell. 2010; 140:951–951. e952. [PubMed: 20303882]
2. Steinhubl SR. Why have antioxidants failed in clinical trials? Am J Cardiol. 2008; 101:14D–19D.
3. Bedard K, Krause KH. The NOX family of ROS-generating NADPH oxidases: physiology and pathophysiology. Physiol Rev. 2007; 87:245–313. [PubMed: 17237347]
4. Dringen R. Oxidative and antioxidative potential of brain microglial cells. Antioxid Redox Signal. 2005; 7:1223–1233. [PubMed: 16115027]
5. Walder CE, et al. Ischemic stroke injury is reduced in mice lacking a functional NADPH oxidase. Stroke. 1997; 28:2252–2258. [PubMed: 9368573]
6. Kleinschnitz C, et al. Post-stroke inhibition of induced NADPH oxidase type 4 prevents oxidative stress and neurodegeneration. PLoS Biol. 2010; 8
7. DeCoursey TE. Voltage-gated proton channels and other proton transfer pathways. Physiol Rev. 2003; 83:475–579. [PubMed: 12663866]
8. DeCoursey TE, Morgan D, Cherny VV. The voltage dependence of NADPH oxidase reveals why phagocytes need proton channels. Nature. 2003; 422:531–534. [PubMed: 12673252]

9. Ramsey IS, Moran MM, Chong JA, Clapham DE. A voltage-gated proton-selective channel lacking the pore domain. Nature. 2006; 440:1213–1216. [PubMed: 16554753]
10. Sasaki M, Takagi M, Okamura Y. A voltage sensor-domain protein is a voltage-gated proton channel. Science. 2006; 312:589–592. [PubMed: 16556803]
11. Okochi Y, Sasaki M, Iwasaki H, Okamura Y. Voltage-gated proton channel is expressed on phagosomes. Biochem Biophys Res Commun. 2009; 382:274–279. [PubMed: 19285483]
12. Ramsey IS, Ruchti E, Kaczmarek JS, Clapham DE. Hv1 proton channels are required for high-level NADPH oxidase-dependent superoxide production during the phagocyte respiratory burst. Proc Natl Acad Sci U S A. 2009; 106:7642–7647. [PubMed: 19372380]
13. Capasso M, et al. HVCN1 modulates BCR signal strength via regulation of BCR-dependent generation of reactive oxygen species. Nat Immunol. 2010; 11:265–272. [PubMed: 20139987]
14. Musset B, et al. A pH-stabilizing role of voltage-gated proton channels in IgE-mediated activation of human basophils. Proc Natl Acad Sci U S A. 2008; 105:11020–11025. [PubMed: 18664579]
15. Iovannisci D, Illek B, Fischer H. Function of the HVCN1 proton channel in airway epithelia and a naturally occurring mutation, M91T. J Gen Physiol. 2010; 136:35–46. [PubMed: 20548053]
16. Lishko PV, Botchkina IL, Fedorenko A, Kirichok Y. Acid extrusion from human spermatozoa is mediated by flagellar voltage-gated proton channel. Cell. 2010; 140:327–337. [PubMed: 20144758]
17. Thomas RC, Meech RW. Hydrogen ion currents and intracellular pH in depolarized voltage-clamped snail neurones. Nature. 1982; 299:826–828. [PubMed: 7133121]
18. De Simoni A, Allen NJ, Attwell D. Charge compensation for NADPH oxidase activity in microglia in rat brain slices does not involve a proton current. Eur J Neurosci. 2008; 28:1146–1156. [PubMed: 18783372]
19. Schilling T, Eder C. Ion channel expression in resting and activated microglia of hippocampal slices from juvenile mice. Brain Res. 2007; 1186:21–28. [PubMed: 18005942]
20. DeCoursey TE. Voltage-gated proton channels: what's next? J Physiol. 2008; 586:5305–5324. [PubMed: 18801839]
21. Visentin S, Agresti C, Patrizio M, Levi G. Ion channels in rat microglia and their different sensitivity to lipopolysaccharide and interferon-gamma. J Neurosci Res. 1995; 42:439–451. [PubMed: 8568930]
22. Cheng YM, Kelly T, Church J. Potential contribution of a voltage-activated proton conductance to acid extrusion from rat hippocampal neurons. Neuroscience. 2008; 151:1084–1098. [PubMed: 18201832]
23. Boron WF, De Weer P. Intracellular pH transients in squid giant axons caused by CO2, NH3, and metabolic inhibitors. J Gen Physiol. 1976; 67:91–112. [PubMed: 1460]
24. Davalos D, et al. ATP mediates rapid microglial response to local brain injury in vivo. Nat Neurosci. 2005; 8:752–758. [PubMed: 15895084]
25. Wu LJ, Vadakkan KI, Zhuo M. ATP-induced chemotaxis of microglial processes requires P2Y receptor-activated initiation of outward potassium currents. Glia. 2007; 55:810–821. [PubMed: 17357150]
26. Block ML, Zecca L, Hong JS. Microglia-mediated neurotoxicity: uncovering the molecular mechanisms. Nat Rev Neurosci. 2007; 8:57–69. [PubMed: 17180163]
27. Gambhir SS, et al. A tabulated summary of the FDG PET literature. J Nucl Med. 2001; 42:1S–93S. [PubMed: 11483694]
28. Lyons SA, et al. Distinct physiologic properties of microglia and blood-borne cells in rat brain slices after permanent middle cerebral artery occlusion. J Cereb Blood Flow Metab. 2000; 20:1537–1549. [PubMed: 11083228]
29. Kraft R, et al. Hydrogen peroxide and ADP-ribose induce TRPM2-mediated calcium influx and cation currents in microglia. Am J Physiol Cell Physiol. 2004; 286:C129–C137. [PubMed: 14512294]
30. Whittingham TS, Lust WD, Passonneau JV. An in vitro model of ischemia: metabolic and electrical alterations in the hippocampal slice. J Neurosci. 1984; 4:793–802. [PubMed: 6323646]

31. Brennan AM, et al. NADPH oxidase is the primary source of superoxide induced by NMDA receptor activation. Nat Neurosci. 2009; 12:857–863. [PubMed: 19503084]
32. Chan PH. Reactive oxygen radicals in signaling and damage in the ischemic brain. J Cereb Blood Flow Metab. 2001; 21:2–14. [PubMed: 11149664]
33. Lai AY, Todd KG. Microglia in cerebral ischemia: molecular actions and interactions. Can J Physiol Pharmacol. 2006; 84:49–59. [PubMed: 16845890]
34. Yenari MA, Kauppinen TM, Swanson RA. Microglial activation in stroke: therapeutic targets. Neurotherapeutics. 2010; 7:378–391. [PubMed: 20880502]
35. Liu R, et al. Reversal of age-related learning deficits and brain oxidative stress in mice with superoxide dismutase/catalase mimetics. Proc Natl Acad Sci U S A. 2003; 100:8526–8531. [PubMed: 12815103]
36. Jin R, Yang G, Li G. Inflammatory mechanisms in ischemic stroke: role of inflammatory cells. J Leukoc Biol. 2010; 87:779–789. [PubMed: 20130219]
37. Lalancette-Hebert M, Gowing G, Simard A, Weng YC, Kriz J. Selective ablation of proliferating microglial cells exacerbates ischemic injury in the brain. J Neurosci. 2007; 27:2596–2605. [PubMed: 17344397]
38. Sorce S, Krause KH. NOX enzymes in the central nervous system: from signaling to disease. Antioxid Redox Signal. 2009; 11:2481–2504. [PubMed: 19309263]
39. Schilling M, et al. Microglial activation precedes and predominates over macrophage infiltration in transient focal cerebral ischemia: a study in green fluorescent protein transgenic bone marrow chimeric mice. Exp Neurol. 2003; 183:25–33. [PubMed: 12957485]
40. Gelderblom M, et al. Temporal and spatial dynamics of cerebral immune cell accumulation in stroke. Stroke. 2009; 40:1849–1857. [PubMed: 19265055]
41. Ransohoff RM. Microgliosis: the questions shape the answers. Nat Neurosci. 2007; 10:1507–1509. [PubMed: 18043584]
42. Iadecola C, Anrather J. The immunology of stroke: from mechanisms to translation. Nat Med. 2011; 17:796–808. [PubMed: 21738161]
43. Moskowitz MA, Lo EH, Iadecola C. The science of stroke: mechanisms in search of treatments. Neuron. 2010; 67:181–198. [PubMed: 20670828]
44. Jung S, et al. Analysis of fractalkine receptor CX(3)CR1 function by targeted deletion and green fluorescent protein reporter gene insertion. Mol Cell Biol. 2000; 20:4106–4114. [PubMed: 10805752]
45. Wu LJ, Zhuo M. Resting microglial motility is independent of synaptic plasticity in mammalian brain. J Neurophysiol. 2008; 99:2026–2032. [PubMed: 18256162]
46. Longa EZ, Weinstein PR, Carlson S, Cummins R. Reversible middle cerebral artery occlusion without craniectomy in rats. Stroke. 1989; 20:84–91. [PubMed: 2643202]
47. Fisher M, et al. Update of the stroke therapy academic industry roundtable preclinical recommendations. Stroke. 2009; 40:2244–2250. [PubMed: 19246690]
48. Hara H, Huang PL, Panahian N, Fishman MC, Moskowitz MA. Reduced brain edema and infarction volume in mice lacking the neuronal isoform of nitric oxide synthase after transient MCA occlusion. J Cereb Blood Flow Metab. 1996; 16:605–611. [PubMed: 8964799]
49. Zhao H, et al. Superoxide reacts with hydroethidine but forms a fluorescent product that is distinctly different from ethidium: potential implications in intracellular fluorescence detection of superoxide. Free Radic Biol Med. 2003; 34:1359–1368. [PubMed: 12757846]
50. Boyarsky G, Ganz MB, Sterzel RB, Boron WF. pH regulation in single glomerular mesangial cells. I. Acid extrusion in absence and presence of HCO3. Am J Physiol. 1988; 255:C844–C856. [PubMed: 2849306]

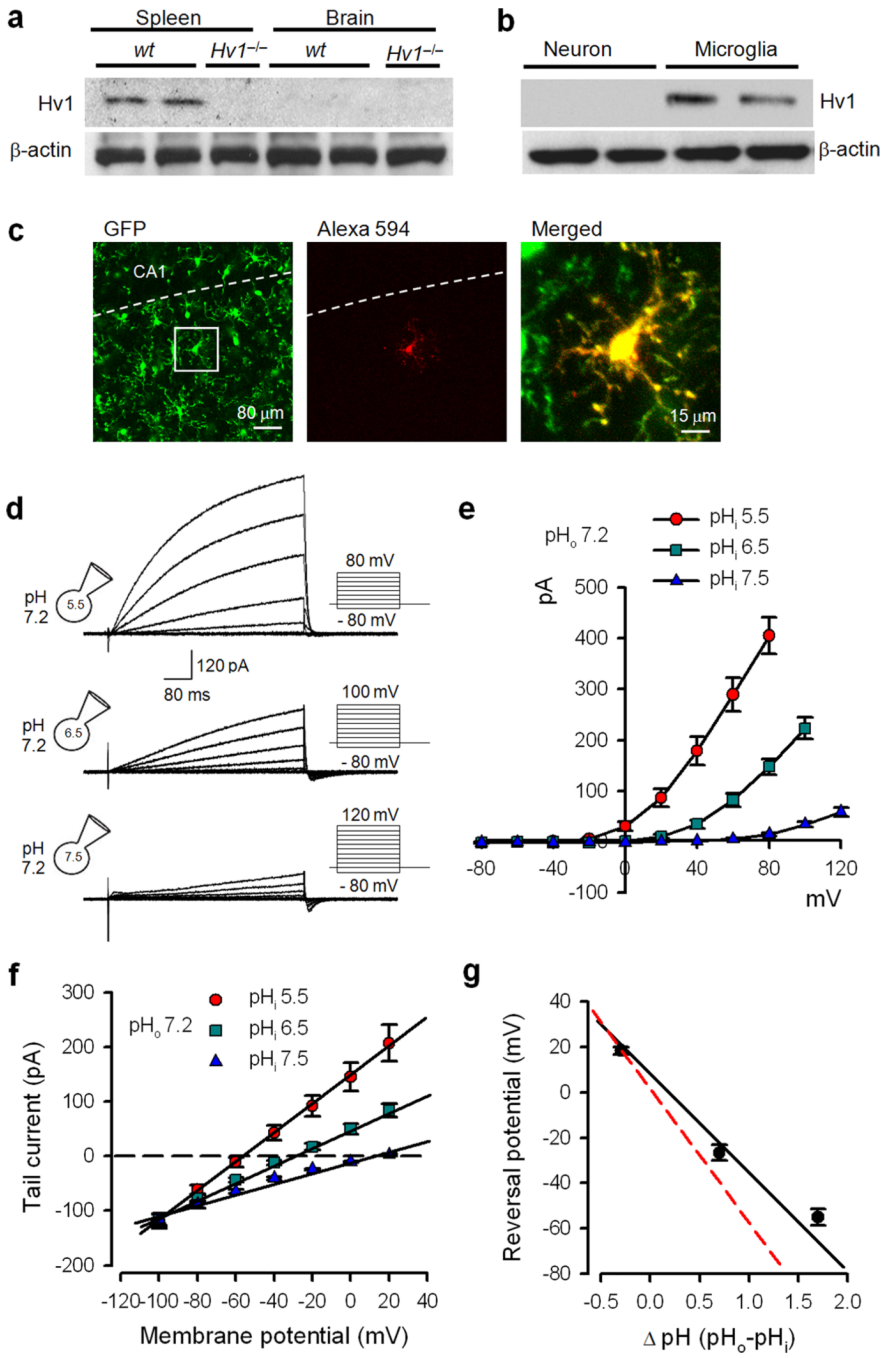

Figure 1. Voltage–gated proton currents in hippocampal microglia in mouse brain slices

(a) Hv1 protein was detected by Western blot (α1–Hv1) in the spleen, but not in whole brain lysates (also see Suppl. Fig. 14a).

(b) Hv1 protein was detected by Western blot (α1–Hv1) in cultured microglia but not in cultured neurons (also see Suppl. Fig. 14b).

(c) A GFP–expressing microglia (shown in white box) in mouse hippocampus labeled with Alexa Fluor 594 prior to whole–cell recording. Dashed line delineates the CA1 region of the hippocampus.

(d) Outward currents induced by voltage steps in hippocampal microglia. Inset: Stimulation protocol and intra– and extracellular pH (pH_i and pH_o). Increased intracellular pH decreased the outward current and shifted the activation threshold to more depolarized potentials.
(e) Pooled data of current–voltage relationships at pH_i 5.5, 6.5 and 7.5; pH_o=7.2. Current amplitude was measured at the end of the 500ms depolarization pulse (n=8–10).
(f) Reversal potentials were determined by tail current recordings. The tail current was recorded at various potentials from –100mV to +20mV after activation of the outward current by a voltage step to +60mV for 1 s (n=7).
(g) Plot of the current reversal potential at different pH_o/pH_i gradients. Data were fitted by a continuous line with a slope of –38mV/ΔpH. The Nernst potential for a proton–selective membrane has a slope of –58mV/ΔpH (red line). Differences from the predicted Nernst relation are due to proton depletion[7].
Data are mean ± s.e.m.

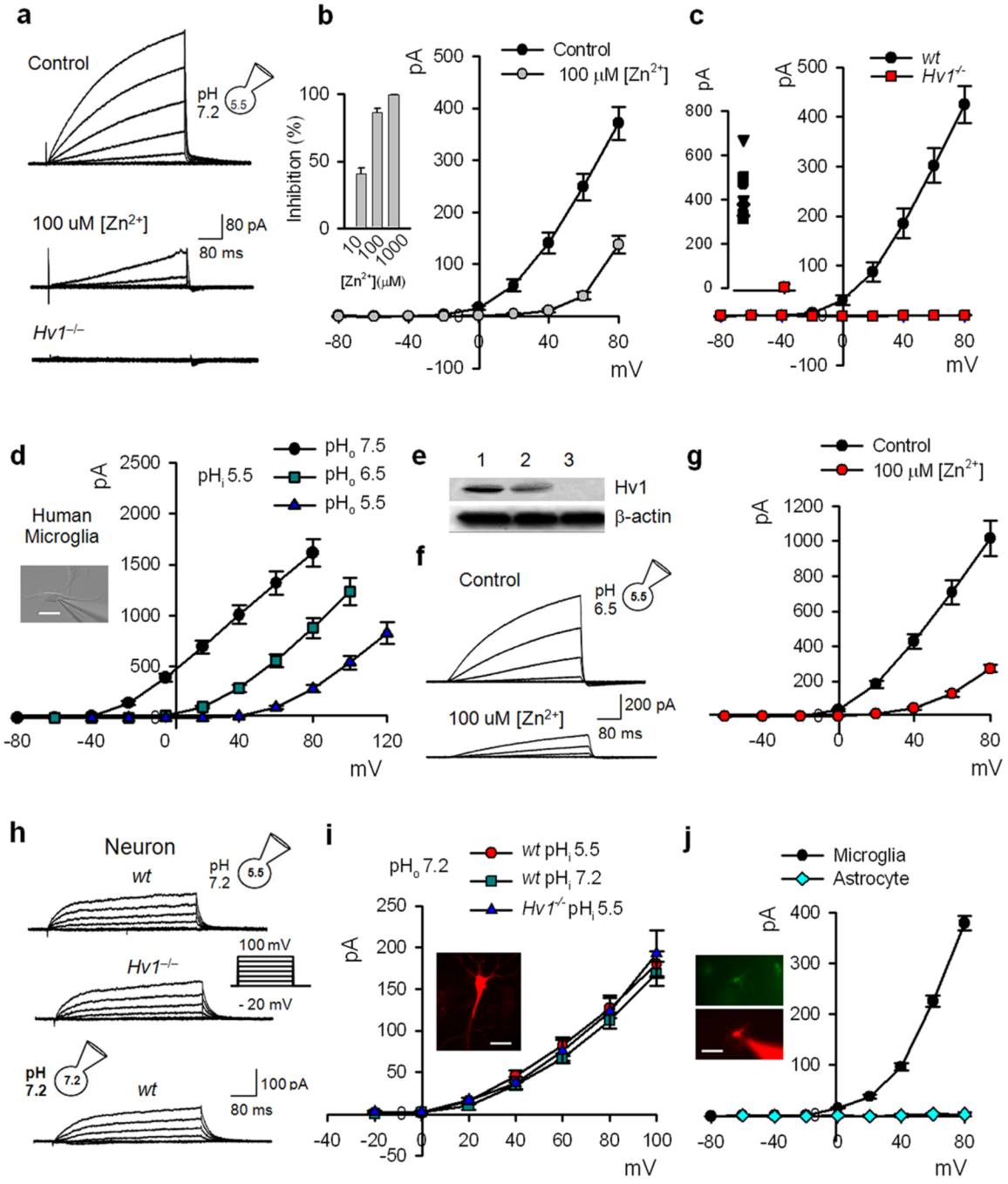

Figure 2. Hv1 mediates the voltage–gated proton current in mouse brain microglia but not in neurons or astrocytes

(a) Inhibition of outward current by 100μM Zn^2; from microglia (pH_o7.2/pH_i5.5) in a hippocampal brain slice. No outward current was observed in *Hv1*$^{-/-}$ microglia.

(b) Voltage–gated proton current amplitudes in control solution or with100μM Zn^{2+}. Zn^{2+} shifts the Hv1 activation threshold. *Inset:* concentration–dependent inhibition by Zn^{2+} at +60mV (n=6).

(c) Absence of proton current in *Hv1*$^{-/-}$ hippocampal microglia. *Inset:* currents at +80mV (n=8 *wt*, *6 Hv1*$^{-/-}$).

(d) Increasing pH_o increases voltage–gated proton current in human microglia (n=9–11). *Inset*: microglia, scale bar, 50μm.
(e) Hv1 protein in human microglia (2). *Wt* (1) and *Hv1*$^{-/-}$ (3) mouse spleens were used as control. α1–Hv1 antibody was used (also see Suppl. Fig. 14c).
(f) 100μM Zn^{2+} inhibits proton current in human microglia.
(g) Pooled results show the Zn^{2+} inhibition of voltage–current relationship of proton current in human microglia (n=8).
(h) Whole–cell currents (primarily Kv) in hippocampal CA1 neurons (pH_o7.2/pH_i5.5; *wt* and *Hv1*$^{-/-}$ neurons) and pH_o7.2/pH_i7.2 (*wt* neurons).
(i) Outward K^+ current amplitudes in *wt* and *Hv1*$^{-/-}$ hippocampal neurons are not different. Currents were not substantially altered by varying pH_i (n=6–7 for each group). *Inset:* CA1 neuron labeled with Alexa Fluor 594 during recording. Scale bar, 80μm.
(j) No proton current was recorded in astrocytes from P3 mice (n=7). *Inset:* GFP–positive astrocyte labeled with Alexa Fluor 594 during recording. Scale bar, 80μm.
Data are mean ± s.e.m.

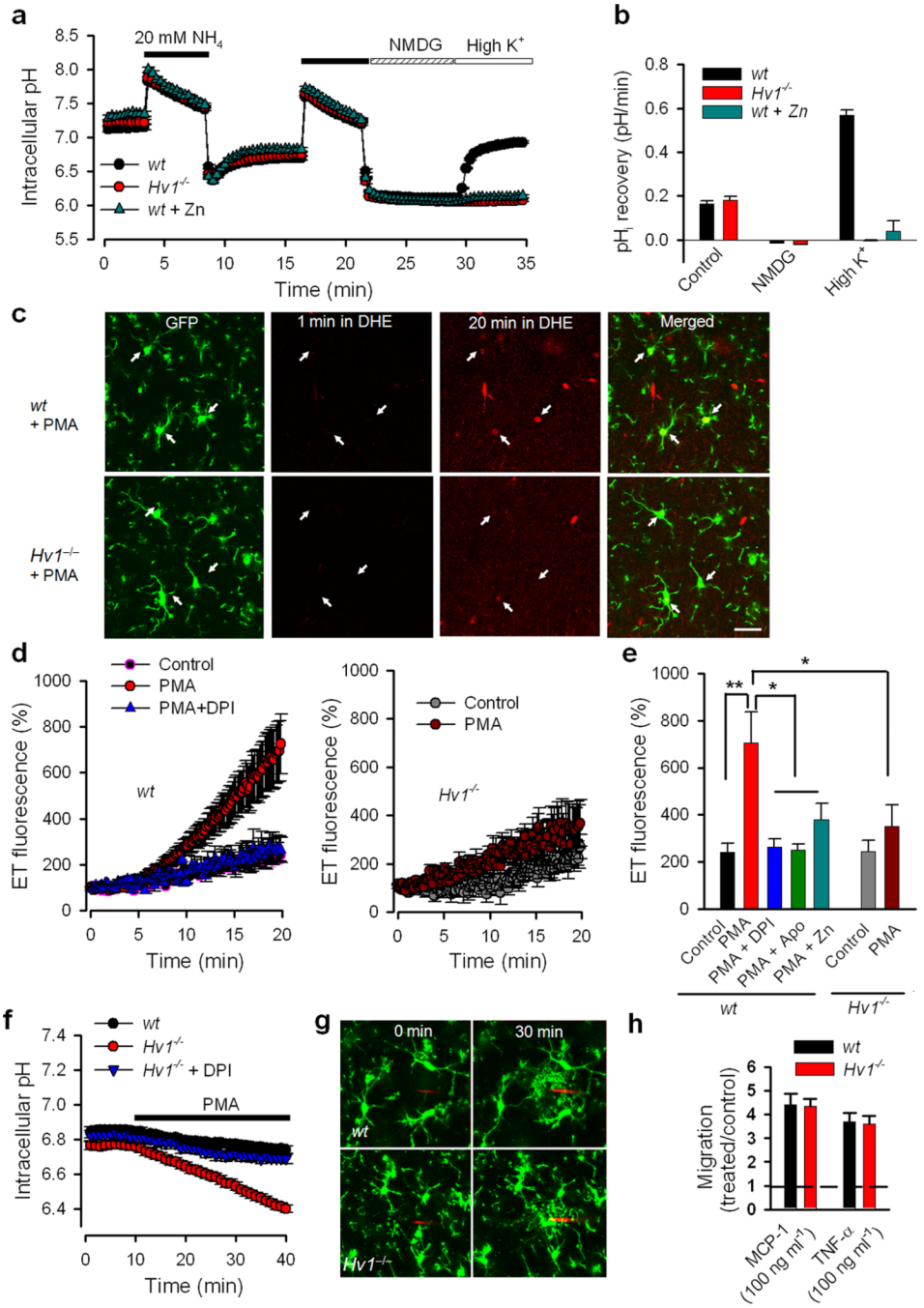

Figure 3. Hv1 regulates microglial acid extrusion and controls NADPH oxidase–dependent ROS production in situ

(a) Intracellular pH (pH_i) change of *wt* (n=29) or $Hv1^{-/-}$ microglia (n=23) in response to NH_4^+–induced acid load, and pH_i recovery in control high Na^+ solution, Na^+–free solution, and Na^+–free, high-K^+ solution. High K^+–induced pH_i recovery in *wt* microglia inhibited by Zn^{2+} (n=16).

(b) pH_i recovery rate (first min) after NH_4^+–induced acid load.

(c) PMA–induced ROS production in microglia (arrows) from $Cx3cr1^{GFP/+}$ and $Cx3cr1^{GFP/+}$– $Hv1^{-/-}$ mice. ROS converts DHE to fluorescent ethidium (ET, red) bar = 20 microns.

(d) Increased ROS in *wt* (*left*, n=11 controls; 13 PMA–treated) and $Hv1^{-/-}$ (*right*, n=7 controls and 8 PMA–treated) microglia. 30μM DPI reduced ROS increase in *wt* (brain slices; n=6).
(e) DPI, apocynin (Apo) or Zn^{2+} reduced ET fluorescence in PMA–stimulated *wt* microglia. PMA–induced ROS was in $Hv1^{-/-}$ was half that of PMA–stimulated *wt* microglia.
(f) pH_i in response to PMA treatment in *wt* (n=30) and $Hv1^{-/-}$ microglia (n=48). Na^+–free solution blocked Na^+–dependent acid extrusion. PMA–induced intracellular acidification was inhibited by DPI (n=25).
(g) ATP–induced terminal chemotaxis was comparable between *wt* (upper) and $Hv1^{-/-}$ (lower) mice (n=3). Alexa Fluor 594 in pipette (red).
(h) Migration in response to 100ng/ml MCP–1 or 100ng/ml TNFα in microglia from *wt* or $Hv1^{-/-}$ mice (n=3). Microglia migrating to the lower well (containing MCP–1 or TNFα) normalized to those migrating without chemoattractant.
Data are mean ± s.e.m.

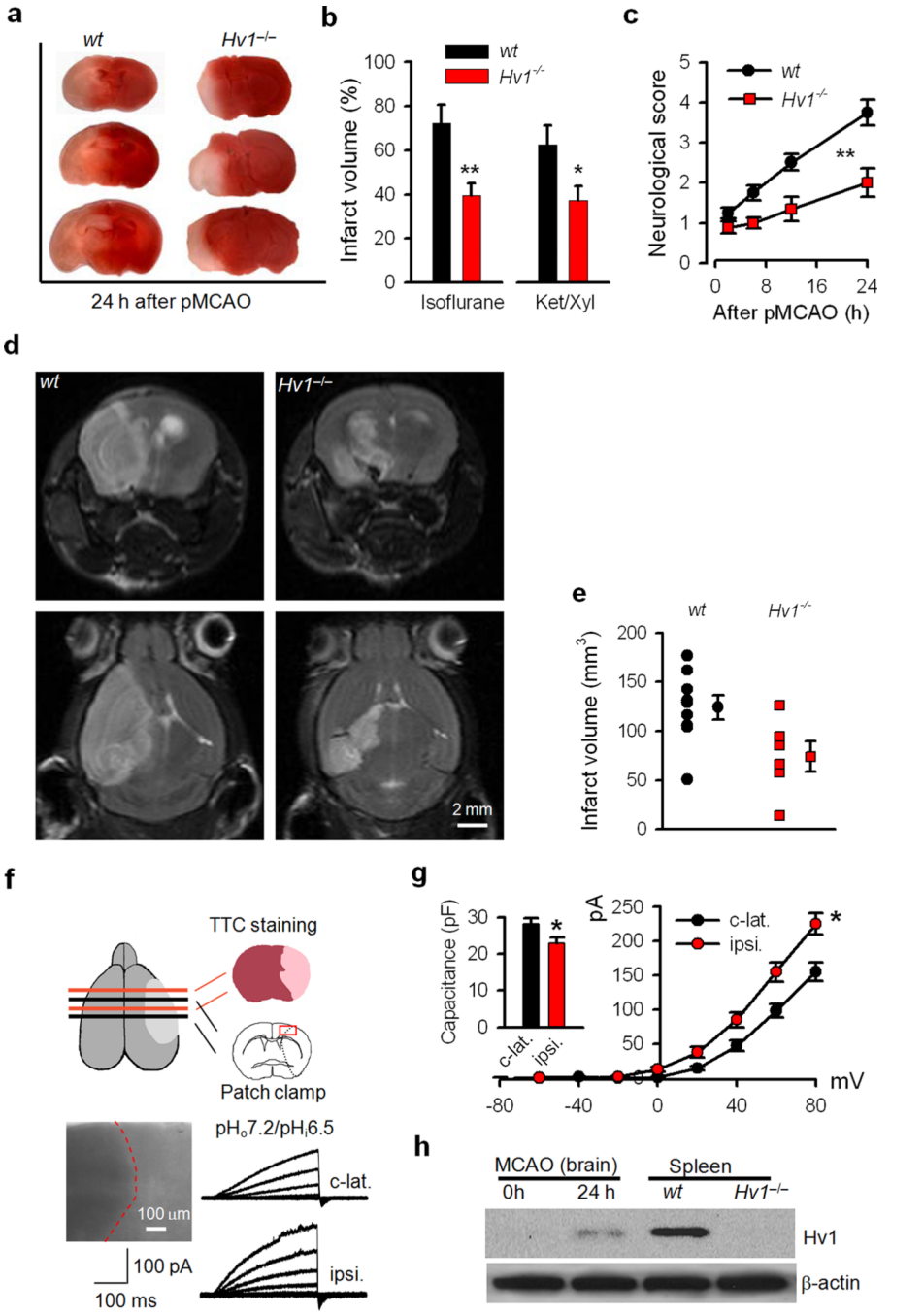

Figure 4. *Hv1*$^{-/-}$ mice are protected in ischemic stroke

(a) TTC staining of coronal brain sections of *wt* and *Hv1*$^{-/-}$ mice 24h after pMCAO under isoflurane.

(b) Infarct volume was reduced from 72.3±8.4% in *wt* mice (n=7) to 39.4±5.8% of total brain in *Hv1*$^{-/-}$ mice (n=7); isoflurane anesthesia. Smaller infarct volumes in *Hv1*$^{-/-}$ mice (37±7%, n=11) than that in *wt* mice (62±8%, n=12) after pMCAO; ketamine/xylazine (Ket/Xyl) anesthesia.

(c) Neurological scores after pMCAO showing less neurological impairment in *Hv1*$^{-/-}$ mice (n=11) than *wt* mice (n=12).

(d) Coronal (upper) and transverse (lower) MRI brain images from *wt* and *Hv1*$^{-/-}$ mice 24h after pMCAO.
(e) Infarct volumes measured based on coronal MRI images. Individual and pooled data; infarct volume in *Hv1*$^{-/-}$ mice (124.3±12.3 mm^3; n=6) was ~60% of that in *wt* mice (74.1±15.5 mm^3; n=7).
(f) Experimental procedure: 1d after pMCAO, the mouse brain was sliced, stained by TTC, and microglia within the slice recorded. TTC staining shows peri-infarct area (seen also in DIC, dotted red line, *lower, left*). Whole-cell recording of voltage–gated proton currents from ipsilateral (ipsi.) and contralateral (c–lat.) microglia after pMCAO (pH_o7.2/pH_i6.5) (*lower, right*).
(g) Increase of voltage–gated proton currents in ipsilateral microglia compared to contralateral controls. *Inset:* Microglial cell surface area (cell capacitance; pF), was smaller in ipsilateral (ipsi.) than contralateral (c–lat.) microglia (n=6).
(h) Hv1 protein (α2–Hv1) increased 24h after pMCAO (also see Suppl. Fig. 14d). Spleen was the control (n =3).
Data are mean ± s.e.m.

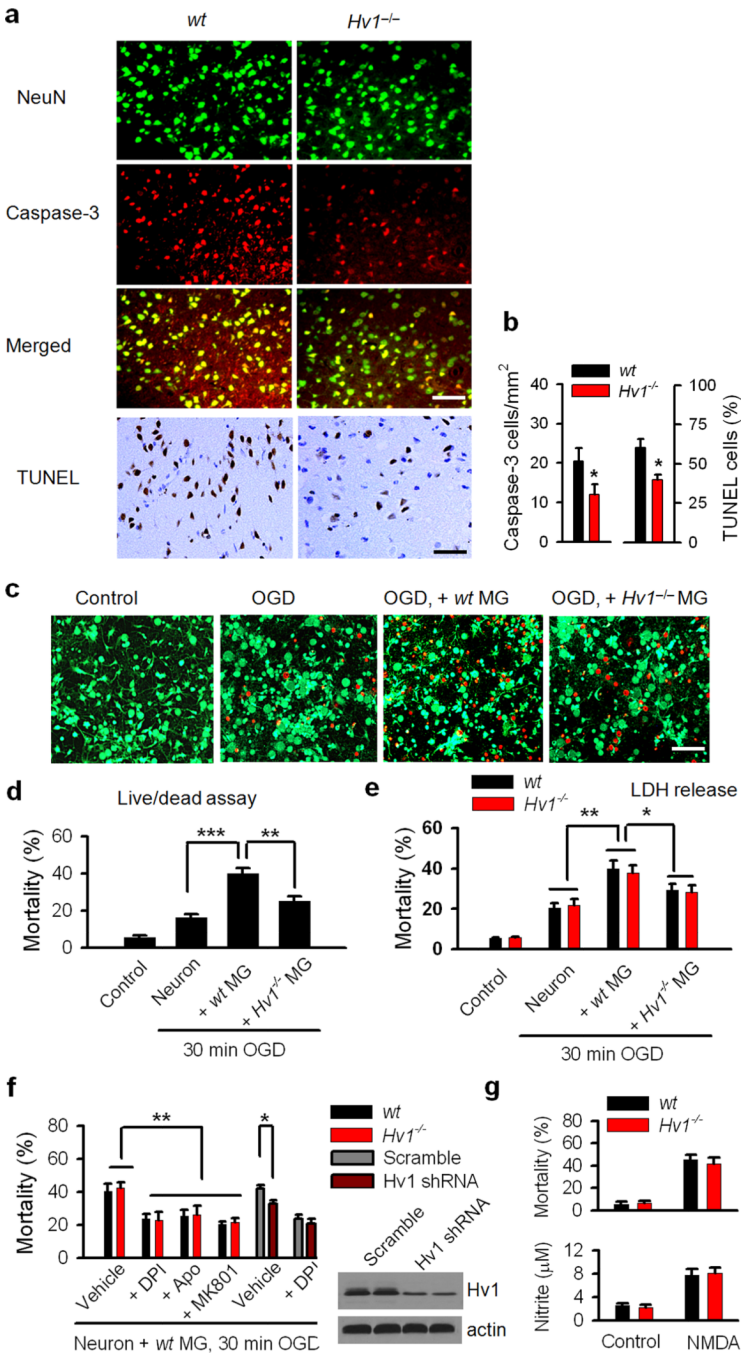

Figure 5. Hv1–deficient mice are relatively protected against ischemic neuronal death

(a) NeuN, cleaved caspase–3, and TUNEL immunostaining of peri–infarct cortex from *wt* and *Hv1*$^{-/-}$ mice 24 h after pMCAO. Scale bars=120 μm.

(b) Pooled data showing significant fewer caspase–3 positive neurons and TUNEL positive cells after ischemic stroke in *Hv1*$^{-/-}$ mice compared to *wt* mice (n=3).

(c) Oxygen glucose deprivation (OGD) reduced cell viability as assayed by live/dead cell staining with EthD–1 and calcein–AM. Green=live cells; red=membrane permeant (dead) cells. MG, microglia. Scale bar =120μm.

(d) Cell mortality was calculated from live/dead assay as shown in (d). Addition of *Hv1*$^{-/-}$ microglia to neuronal cultures resulted in less OGD–induced cell death than addition of *wt* microglia (n=3). Cell counts insured equal numbers of microglia added to each culture.
(e) Cell mortality was calculated based on measurement of lactate dehydrogenase (LDH) release. *Wt* and *Hv1*$^{-/-}$ neurons exhibited similar sensitivity to OGD (n=3).
(f) Microglia–related OGD–induced cell mortality (based on LDH release) was inhibited by DPI, apocynin (Apo), MK801, or by Hv1 shRNA knockdown. *Inset* shows Hv1 protein expression (α1–Hv1) in microglia treated with scrambled or Hv1 shRNA for 3d (also see Suppl. Fig. 14e).
(g) NMDA–induced cell death (upper) or NO release (lower) is comparable between *wt* and *Hv1*$^{-/-}$ neurons.
Data are mean ± s.e.m.

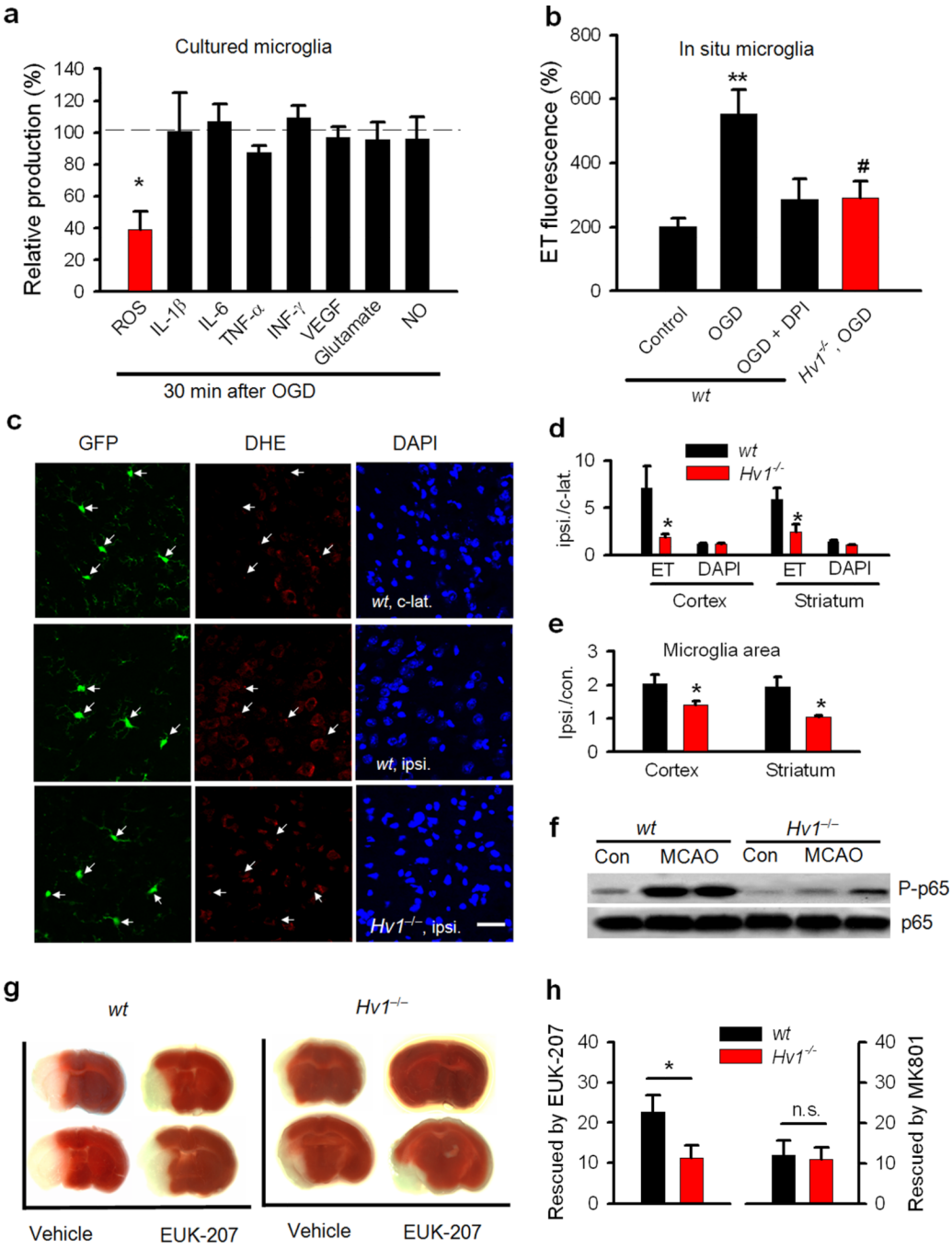

Figure 6. Microglial Hv1 is critical for ROS production after stroke

(a) Production of ROS and release of glutamate, NO, and cytokines (IL–1β, IL–6, TNFα, INF–γ, VEGF) 30min after OGD from cultured *wt* and *Hv1*$^{-/-}$ microglia (n=3). Normalized to *wt*.

(b) Microglia ROS production (ET fluorescence) in brain slices. OGD increased ROS production in *wt* microglia (n=8) significantly more than in *Hv1*$^{-/-}$ microglia (n =7).

(c) Microglial ROS production *in situ* detected by i.p. injection of DHE after tMCAO. Microglia were identified by GFP; nuclei in the peri–infarct cortex identified by DAPI. Scale bar=30 μm.

(d) Microglial ROS production in *Hv1*$^{-/-}$ mice was increased in ipsilateral (ipsi.) compared to contralateral brain (n=13; c–lat. Side, 21; ipsi.) and compared to *wt* mice (n=15; c–lat., 20; ipsi.). Microglial ROS production: ratio of ET intensity from ipsi. and c–lat. brain. DAPI intensity in *wt* and *Hv1*$^{-/-}$ mice not significantly different. Results in cortex and striatum are similar.
(e) Cell body areas of GFP–labeled microglia measured from *wt* and *Hv1*$^{-/-}$ mice.
(f) Phosphorylation of p65 (P–p65) increased more in *wt* mice than in *Hv1*$^{-/-}$ mice after MCAO (also see Suppl. Fig. 14f). No difference in expression of total p65 between *wt* and *Hv1*$^{-/-}$ mice (n=3).
(g) EUK–207 reduced infarct volume 3d after pMCAO in both *wt* and *Hv1*$^{-/-}$ mice (TTC).
(h) EUK–207 rescue of brain damage is greater in *wt* (n=8) than in *Hv1*$^{-/-}$ mice (n=7), while there is no protection by MK801 in *wt* (n=8) and *Hv1*$^{-/-}$ mice (n=9).
Data are mean ± s.e.m.

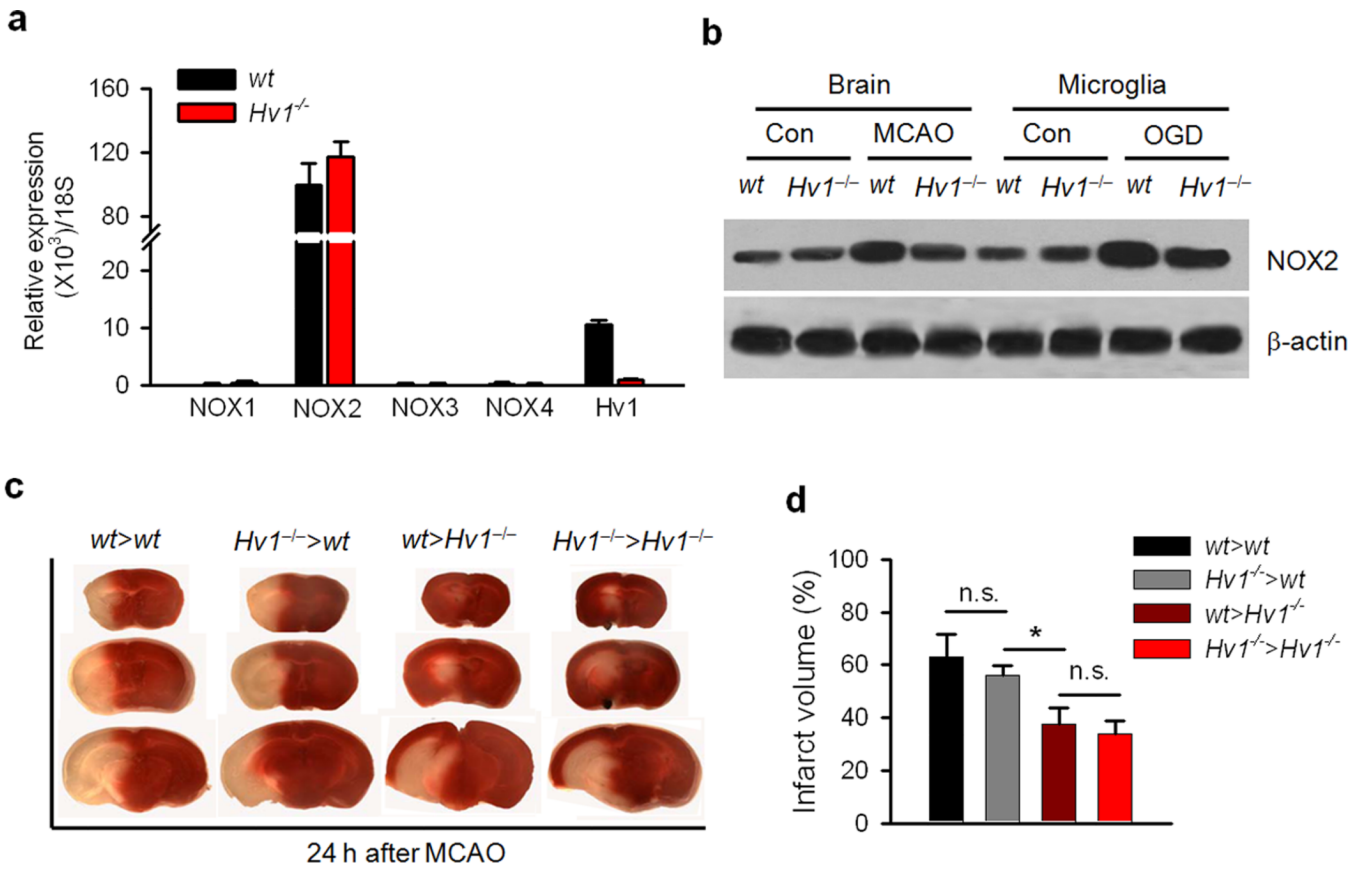

Figure 7. Microglial, but not leukocyte, Hv1 is responsible for brain damage after ischemic stroke

(a) Transcripts of NOX1, NOX2, NOX3, NOX4, Hv1 and 18s rRNA were examined in *wt* and *Hv1*$^{-/-}$ microglia using qRT–PCR. The NOX2 transcript level is similar in *wt* and *Hv1*$^{-/-}$ microglia (n=4 each group).

(b) Western blot showing similar NOX2 expression in *wt* and *Hv1*$^{-/-}$ microglia. After MCAO or OGD, NOX2 expression increased significantly (also see Suppl. Fig. 14g).

(c) Infarct volume (TTC staining) in chimeras of *wt>wt, wt> Hv1*$^{-/-}$*, Hv1*$^{-/-}$*>wt*, and *Hv1*$^{-/-}$*> Hv1*$^{-/-}$ mice.

(d) Pooled data show significantly more brain damage in *Hv1*$^{-/-}$*>wt* mice (n=7) than in *wt>Hv1*$^{-/-}$ mice (n=7).

Data are mean ± s.e.m.